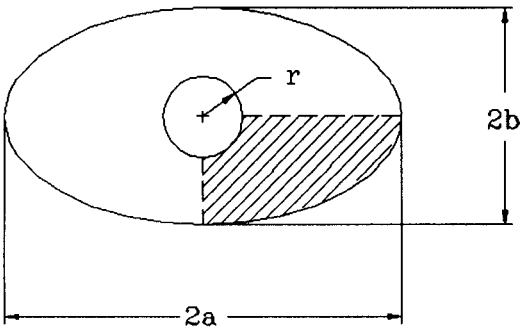

Fig. 3. Outer conductor of elliptical cross section.

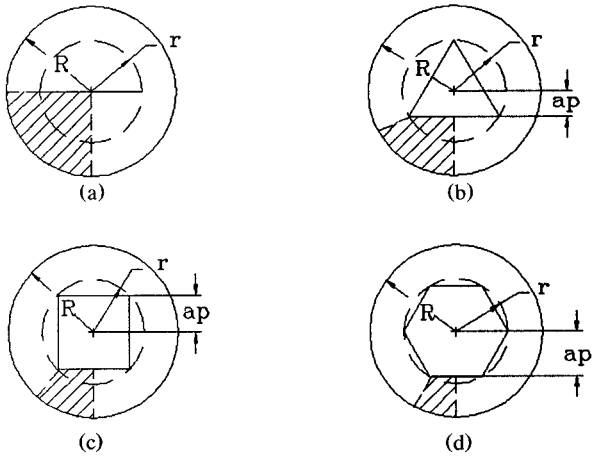

Fig. 4. Inner conductor of regular-polygon cross section for (a) $N = 2$, (b) $N = 3$, (c) $N = 4$, and (d) $N = 6$.

inversion by optimization a general-purpose tool very applicable to a broad range of cases.

Indeed, nearly all the structures examined led to large ratios between adjacent sides in the transformed plane of the optimization. These ratios cannot be handled with traditional techniques, but by developing the integration techniques introduced in [2], ratios up to 10^{15} have been easily faced. Nevertheless, these conformal mapping techniques often require knowledge of magnetic boundary walls which are not immediately suggested by the geometry of the structure.

References

[1] S. G. Pan, "Characteristic impedance of a coaxial system consisting of circular and noncircular conductors," *IEEE Trans. Microwave Theory Tech.*, vol. 36, pp. 917–921, May 1988.

[2] E. Costamagna, "On the numerical inversion of the Schwarz-Christoffel conformal transformation," *IEEE Trans. Microwave Theory Tech.*, vol. MTT-35, pp. 35–40, Jan. 1987.

[3] M. A. R. Gunston, *Microwave Transmission-Line Impedance Data*. London: Van Nostrand Reinhold, 1972.

[4] H. A. Wheeler, "Transmission-line properties of a round wire in polygon shield," *IEEE Trans. Microwave Theory Tech.*, vol. MTT-27, pp. 717–721, Aug. 1979.

[5] T. K. Seshadri and K. Rajaiah, "Accurate estimation of characteristic impedance of coaxial transmission-line problems by eigenfunction approach," *Proc. IEEE*, vol. 70, pp. 82–84, Jan. 1982.

[6] L. N. Epele, H. Fanchiotti, and C. A. García Canal, "Characteristic impedance of coaxial lines bounded by N-regular polygons," *Proc. IEEE*, vol. 72, pp. 223–224, Feb. 1984.

[7] H. J. Riblet, "An accurate approximation of the impedance of a circular cylinder concentric with an external square tube," *IEEE Trans. Microwave Theory Tech.*, vol. MTT-31, pp. 841–844, Oct. 1983.

[8] N. Seshagiri, "Least-weighted-square method for the analysis and synthesis of transmission lines," *IEEE Trans. Microwave Theory Tech.*, vol. MTT-15, pp. 494–503, Sept. 1967.

[9] W. G. Lin and S. L. Chung, "A new method of calculating the characteristic impedances of transmission lines," *Acta Phys. Sin.*, vol. 19, pp. 249–258, Apr. 1963 (in Chinese). Selected results are quoted in [1, p. 66].

[10] S. G. Pan, "A method of solving coaxial transmission lines of complicated cross-section," *Scientia Sinica*, series A, pp. 205–217, Feb. 1987.

[11] R. M. Chisholm, "The characteristic impedance of trough and slab lines," *IRE Trans. Microwave Theory Tech.*, vol. MTT-4, pp. 166–172, July 1956.

[12] T. K. Seshadri and K. Rajaiah, "Eigenfunction solutions of a class of TEM transmission line," *Proc. Inst. Elec. Eng.*, vol. 131, pt. H, pp. 279–280, Aug. 1984.

[13] W. Lin, "A critical study of the coaxial transmission line utilizing conductors of both circular and square cross-section." *IEEE Trans. Microwave Theory Tech.*, vol. MTT-30, pp. 1981–1988, Nov. 1982.

[14] F. Oberhettinger and W. Magnus, *Applications of Elliptic Functions in Physics and Technology*. New York: Springer, 1949.

[15] W. Geyi, L. Xueguan, and W. Wanchun, "Solution of the characteristic impedance of an arbitrarily shaped TEM transmission line using complex variable boundary element method (CVBEM)," *Proc. Inst. Elec. Eng.*, vol. 136, pt. H, pp. 73–75, Feb. 1989.

[16] H. J. Riblet, "The exact dimensions of a family of rectangular coaxial lines with given impedance," *IEEE Trans. Microwave Theory Tech.*, vol. MTT-20, pp. 538–541, Aug. 1972.

A Procedure for Solving the Electric Field Integral Equation for a Dielectric Scatterer with a Large Permittivity Using Face-Centered Node Points

Ching-Chuan Su

Abstract—**A numerical procedure for solving the electric field integral equation (EFIE) using the pulse-basis block model is proposed. The main features of the method are the use of face-centered node points and a unique way of choosing the unknown fields. Such a procedure keeps the resulting matrix relatively well conditioned, even when the magnitude of the permittivity is large. In addition, the proposed procedure can preserve the convolution property contained in the EFIE and, hence, the FFT can be incorporated into the algorithm.**

I. Introduction

The electric field integral equation (EFIE) is widely employed to analyze inhomogeneous dielectric scatterers of arbitrary shapes. To solve the integral equation numerically the method employing the block model (i.e., using rectangular cells to model an arbitrarily shaped scatterer) in conjunction with the pulse-function expansion and the point-matching technique is rather popular [1]–[7]. Recently, the efficiency of this method with respect to both computational speed and memory requirements has been greatly improved by the use of the conjugate gradient method (CGM) and the fast Fourier transform (FFT) [4]–[6].

Manuscript received March 1, 1990; revised December 31, 1990.

The author is with the Department of Electrical Engineering, National Tsinghua University, Hsinchu, Taiwan.

IEEE Log Number 9144275.

However, except for the two-dimensional TM (transverse magnetic) scattering cases, the conventional procedure for solving the EFIE using the pulse-basis block model has one fatal drawback: the relative permittivity of the scatterer must be kept small (of order unity). Otherwise, the iterative CGM converges very slowly or may even stagnate [5]–[7]. Even if a solution is obtained using the CGM or other methods, it may contain serious errors [7]–[9]. These errors are believed to be due to a term in the EFIE representing the effect of induced polarization charge [5]. (Note that such a term does not emerge in the TM scattering.) It has been indicated that, in the presence of such a charge term, the magnitudes of off-diagonal elements and hence the condition numbers of the resulting matrices increase as the permittivities are increased [5]. Remark that in the matrix equation $\boldsymbol{Ax} = \boldsymbol{b}$ the condition number c of matrix $\boldsymbol{A}$ is a measure of the sensitivity of solution $\boldsymbol{x}$ due to sight variation in matrix $\boldsymbol{A}$ or vector $\boldsymbol{b}$. For a well-conditioned matrix, c is close to unity; for an ill-conditioned one, $c \gg 1$. A more detailed discussion of the condition number is given in Section V. The accuracy may be improved if more sophisticated approaches are used (to reduce the error in matrix $\boldsymbol{A}$), for example evaluating matrix elements elaborately [5], [6], [8], [10], modeling the scatterer accurately by using more flexible cells [8], [11]–[13], and employing higher order basis functions [11]–[13]. However, these approaches are not necessarily workable for scatterers with large permittivities (for example, see [8]). Moreover, the use of sophisticated cell structures and/or basis functions may degrade the convolution property contained in the EFIE. Thus, the efficient FFT cannot be applied and the memory requirement is prohibitively large.

In order to solve the EFIE using the simple pulse-basis block model, a new procedure is proposed. The main features of this procedure are the following two steps:

1) Face-centered node points are used. That is, the node points at which the fields are to be sampled are not placed at the center of each block, as conventionally done, but are placed at the centers of the faces of each block. Such an approach should represent the polarization charges induced at the faces more accurately, especially at larger permittivity discontinuities around which the electric field varies rapidly.
2) The unknown fields at the face-centered node points are chosen in a unique way to ensure that the magnitudes of off-diagonal elements of the resulting matrix are small, regardless of the magnitudes of the permittivities involved. Such an approach will keep the condition number of the resulting matrix small, even when the magnitudes of the permittivities are large.

In this investigation we consider the two-dimensional case, where exact solutions for the electric field distributions inside circular homogeneous cylinders are available and can be used to check the calculated results. The numerical procedure discussed in Sections III and IV can be generalized to the three-dimensional case.

II. Electric Field Integral Equation

Consider the TE (transverse electric) scattering from an isotropic dielectric cylinder with an arbitrary relative permittivity distribution $\epsilon(x, y)$ exposed to an incident field $\boldsymbol{E}^i(x, y)$ polarized in the $x-y$ plane. The resultant electric field $\boldsymbol{E}(x, y) = \hat{x}E_x(x, y) + \hat{y}E_y(x, y)$ can be found from the magnetic vector and electric scalar potentials, which are due to the polarization current and polarization charge densities, respectively; that is,

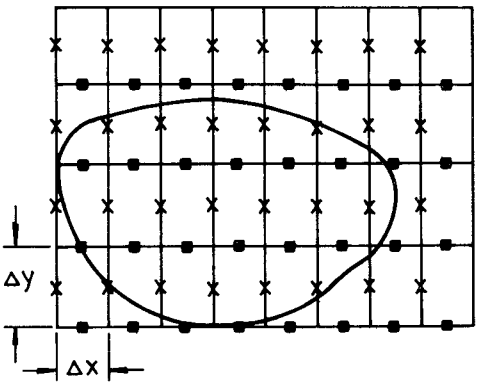

Fig. 1. A rectangular mesh with $m_1 \times m_2$ identical cells of size Δx by Δy. The $(m_1-1)\times(m_2-1)$ cells should cover the cylinder's cross section.

$$\boldsymbol{E}(x, y) = \boldsymbol{E}^i(x, y) + k^2 \int\int G(k\rho)\{[\epsilon(x', y') - 1]\boldsymbol{E}(x', y')\}\, dx'dy' - \frac{1}{\epsilon_0}\nabla \int\int G(k\rho)\rho_c(x', y')\, dx'dy'. \tag{1}$$

Here $\nabla = \hat{x}\partial/\partial x + \hat{y}\partial/\partial y$, the two-dimensional free-space Green's function $G(k\rho) = H_0^{(2)}(k\rho)/4j$, $\rho^2 = (x-x')^2 + (y-y')^2$, $k^2 = \omega^2\mu_0\epsilon_0$, and ρ_c denotes the induced polarization charge density, which can be expressed in several ways:

$$\rho_c(x, y) = -\epsilon_0\nabla\cdot\{[\epsilon(x, y) - 1]\boldsymbol{E}(x, y)\} \tag{2a}$$

$$= \epsilon_0\nabla\cdot\boldsymbol{E}(x, y) \tag{2b}$$

$$= -\epsilon_0\frac{\nabla\epsilon(x, y)}{\epsilon(x, y)}\cdot\boldsymbol{E}(x, y), \tag{2c}$$

where the continuity equation and Gauss's law have been made use of. It is understood that (2b) and (2c) are valid in those regions having no free charge. Different expressions correspond to different formulations. Use of (2a) leads to the commonly used electric field integral equation involving a dyadic Green's function. It is shown in Section V that the condition numbers of the matrices resulting from such a formulation increase as the permittivities are increased.

III. Numerical Procedure for Face-Centered Node Points

The scatterer is modeled by rectangular cells wherein the permittivity within each cell is treated as a constant (namely, the block model). The pulse-function expansion and the point-matching technique are employed in the numerical calculation. The node points at which the EFIE is enforced are placed at the centers of the faces (sides, in the two-dimensional case) of each cell. The x and y components of the electric field are sampled and matched at the points marked with a cross ($\times$) and square ($\blacksquare$), respectively, as depicted in Fig. 1. Note that these fields are the normal components with respect to the corresponding interfaces.

The polarization charge density can be given by (2). In the block model the polarization charges are induced only at the interfaces and can be found from the normal components of the electric fields at the interfaces using (2a) or (2b). At an interface

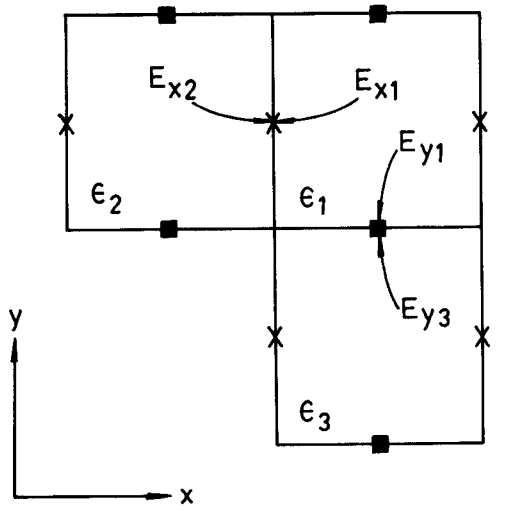

Fig. 2. Fields E_{x1}, E_{x2}, E_{y1}, and E_{y3} denote the normal components at two face-centered node points. From such fields the polarization charges at the node points are determined.

separating two blocks of dissimilar media, the normal component of the electric field is discontinuous. From the continuity of displacement it is known that the normal components of the fields at the respective interfaces satisfy the relations (see Fig. 2 for the locations of the permittivities and field components)

$$\epsilon_1 E_{x1} = \epsilon_2 E_{x2} \tag{3a}$$

and

$$\epsilon_1 E_{y1} = \epsilon_3 E_{y3}. \tag{3b}$$

At an interface separating two blocks of dissimilar media the density becomes impulsive. Using (2b) and (3) the corresponding surface (line, in the two-dimensional case) charge densities ρ_{sx} and ρ_{sy} at the respective face-centered node points are given by

$$\rho_{sx} = \epsilon_0 E_{x2} \frac{\epsilon_2 - \epsilon_1}{\epsilon_1}, \qquad |\epsilon_1| \geq |\epsilon_2| \tag{4a}$$

$$= \epsilon_0 E_{x1} \frac{\epsilon_2 - \epsilon_1}{\epsilon_2}, \qquad \text{otherwise} \tag{4b}$$

and

$$\rho_{sy} = \epsilon_0 E_{y3} \frac{\epsilon_3 - \epsilon_1}{\epsilon_1}, \qquad |\epsilon_1| \geq |\epsilon_3| \tag{4c}$$

$$= \epsilon_0 E_{y1} \frac{\epsilon_3 - \epsilon_1}{\epsilon_3}, \qquad \text{otherwise.} \tag{4d}$$

Unique to this method is that we use either (4a) or (4b) to represent the surface charge density in the integral equation (1) (and, hence, choose either E_{x2} or E_{x1} as the field to be determined) *according to whether* ϵ_1 *or* ϵ_2 *is larger in magnitude*. It is essential to note that the fractions involving the relative permittivities in the chosen formulas are always small in magnitude (ordinarily less than unity). Consequently, the magnitudes of off-diagonal matrix elements can be kept small, regardless of the magnitudes the permittivities involved. In this manner, the node point is not exactly placed at the interface, but approaches the interface from the side where the permittivity is smaller. The same procedure is used to select either E_{y1} or E_{y3} as an unknown field in the integral equation.

To comply with the FFT algorithm we use a rectangular mesh which is composed of $m_1 \times m_2$ identical cells of size Δx by Δy and covers the cross section of the scatterer (see Fig. 1). Then, on applying the point-matching technique at each node point, the integral equation (1) becomes the $2 \times m_1 \times m_2$ simultaneous equations in terms of the $m_1 \times m_2$ fields E_x at the node points marked with a cross and the $m_1 \times m_2$ fields E_y at the node points marked with a square:

$$\begin{aligned} E_x(i,j) = {} & E_x^t(i,j) + s_x(i,j)\chi_1(i,j)E_x(i,j) \\ & + \sum_{q=0}^{m_2-1} \sum_{p=0}^{m_1-1} \{ g(i-p,j-q)\chi_3(p,q)E_x(p,q) \\ & + g_{xx}(i-p,j-q)\chi_1(p,q)E_v(p,q) \\ & + g_{xy}(i-p,j-q)\chi_2(p,q)E_y(p,q) \} \end{aligned} \tag{5a}$$

and

$$\begin{aligned} E_y(i,j) = {} & E_y^t(i,j) + s_y(i,j)\chi_2(i,j)E_y(i,j) \\ & + \sum_{q=0}^{m_2-1} \sum_{p=0}^{m_1-1} \{ g(i-p,j-q)\chi_4(p,q)E_y(p,q) \\ & + g_{yx}(i-p,j-q)\chi_1(p,q)E_x(p,q) \\ & + g_{yy}(i-p,j-q)\chi_2(p,q)E_y(p,q) \} \end{aligned} \tag{5b}$$

where $i = 0,1,\cdots,m_1-1$ and $j = 0,1,\cdots,m_2-1$. In (5) $E_x(i,j)$ and $E_y(i,j)$ denote the field components at the face-centered node points approaching, according to the procedure just described, the left and the bottom sides of cell ij, respectively. $E_x^t(i,j)$ and $E_y^t(i,j)$ denote the x and y components of the incident field at the corresponding node points. The quantities χ_1, χ_2, χ_3, χ_4, g, g_{xx}, g_{xy}, g_{yx}, g_{yy}, s_x, and s_y are defined in what follows.

The functions χ_1 and χ_2 correspond to the effect of the induced polarization charge, and χ_3 and χ_4, of the polarization current. By applying the pulse-function expansion or approximating the normal component of the electric field along an interface by the field at the nearest face-centered node point, $E_x(i,j)$ or $E_y(i,j)$, and using formula (4), we have

$$\chi_1(i,j) = \{\epsilon(i,j) - \epsilon(i-1,j)\} / \epsilon_{x\max} \tag{6a}$$

and

$$\chi_2(i,j) = \{\epsilon(i,j) - \epsilon(i,j-1)\} / \epsilon_{y\max} \tag{6b}$$

where $\epsilon(i,j)$ is equal to the average relative permittivity over the cell ij, and $\epsilon_{x\max}$ and $\epsilon_{y\max}$ denote the greater magnitude between $\epsilon(i,j)$ and $\epsilon(i-1,j)$ and between $\epsilon(i,j)$ and $\epsilon(i,j-1)$, respectively. It is seen that at an interface separating two blocks of similar media, the polarization charge is set to zero automatically, as it should be. In other words the associated fictitious charge [8] appearing in the conventional procedure is eliminated automatically. To calculate the polarization current density, one needs to know the electric field within the cells. By approximating the two components of such a field by the fields at the respective nearest face-centered node point and using relation (3), we have

$$\chi_3(i,j) = \{\epsilon(i,j)\epsilon(i-1,j) - \tfrac{1}{2}[\epsilon(i,j) + \epsilon(i-1,j)]\} / \epsilon_{x\max} \tag{6c}$$

and

$$\chi_4(i,j) = \{\epsilon(i,j)\epsilon(i,j-1) - \tfrac{1}{2}[\epsilon(i,j) + \epsilon(i,j-1)]\} / \epsilon_{y\max}. \tag{6d}$$

In (5) the functions g denote the values of k^2 times an integral of the Green's function over a cell. Since the matrices will be well conditioned, it suffices to use the simple formula [14]

$$g(i,j) = k^2 G(k\rho)\,\Delta x\,\Delta y, \qquad i \neq 0 \quad \text{or} \quad j \neq 0 \tag{7a}$$

$$= -\left[1 + {}_{\jmath} 0.5\pi ka H_1^{(2)}(ka)\right], \qquad i = 0 \quad \text{and} \quad j = 0 \tag{7b}$$

where ${}_{\jmath} = \sqrt{-1}$ (not to be confused with index j), $\rho^2 = (i\Delta x)^2 + (j\Delta y)^2$, and $a^2 = \Delta x\,\Delta y/\pi$. The functions $g_{\mu\nu}$ are given by

$$g_{\mu\nu}(i,j) = \frac{\partial}{\partial \mu} \int G(k\rho)\, d\tilde{\nu} \tag{7c}$$

where $\mu, \nu = x$ or y, $\tilde{\nu} = y'$ if $\nu = x$, $\tilde{\nu} = x'$ if $\nu = y$, ρ denotes the distance between the integration point (x', y') and the associated face-centered node point, and the integral is carried along the left or bottom side of a cell. The g_{xy} and g_{yx} are readily calculated by noting that $\partial G/\partial \mu = -\partial G/\partial \mu'$. For the $g_{xx}(i,j)$ and $g_{yy}(i,j)$ with $i \neq 0$ or $j \neq 0$, numerical integrations were used. For the $g_{xx}(0,0)$ and $g_{yy}(0,0)$, associated derivatives of the Green's function are zero when $\rho \neq 0$, and become singular when $\rho = 0$. Such a singularity is integrable and the result is $\pm\frac{1}{2}$, depending on which side of the interface a face-centered node point approaches [15]. Such indefinite terms degrade the convolution property in the EFIE. To avoid the trouble, we let $g_{xx}(0,0) = g_{yy}(0,0) = 0$ and, accordingly, introduce

$$s_x(i,j) = \tfrac{1}{2}, \qquad |\epsilon(i,j)| \geq |\epsilon(i-1,j)|$$

$$= -\tfrac{1}{2}, \quad \text{otherwise} \tag{7d}$$

and

$$s_y(i,j) = \tfrac{1}{2}, \qquad |\epsilon(i,j)| \geq |\epsilon(i,j-1)|$$

$$= -\tfrac{1}{2}, \quad \text{otherwise.} \tag{7e}$$

It is essential to note that with $\epsilon_{x\max}$ and $\epsilon_{y\max}$ emerging in the denominators of (6a) and (6b), the magnitudes of off-diagonal matrix elements are always kept small, regardless of the magnitude of the permittivity distribution. It is shown in Section V that the condition number of the resulting matrix is relatively small and hence the results are less sensitive to the error in modeling. Thus, the scatterer does not need to be modeled very accurately. As a result, the simple block model in conjunction with the pulse-function expansion and the point-matching technique works well. Moreover, the associated calculation preserves the convolution property in the EFIE, and the FFT can be incorporated into the algorithm.

IV. Main Operations Using CGM and FFT

The conjugate gradient method in conjunction with the FFT algorithm can be used to solve the simultaneous equations (5) [5], [6]. The main computations for each iteration step in the CGM are

$$D_x(i,j) - s_x(i,j)\chi_1(i,j)D_x(i,j) - F_{ij}^{-1} \cdot \left\{F[g]F[\chi_3 D_x] + F[g_{xx}]F[\chi_1 D_x] + F[g_{xy}]F[\chi_2 D_y]\right\} \tag{8a}$$

$$D_y(i,j) - s_y(i,j)\chi_2(i,j)D_y(i,j) - F_{ij}^{-1} \cdot \left\{F[g]F[\chi_4 D_y] + F[g_{yx}]F[\chi_1 D_x] + F[g_{yy}]F[\chi_2 D_y]\right\} \tag{8b}$$

$$R_x(i,j) - s_x(i,j)\chi_1^*(i,j)R_x(i,j) - \chi_3^*(i,j)F_{ij}^{-1}\{F[g]^*F[R_x]\} - \chi_1^*(i,j)F_{ij}^{-1}\left\{F[g_{xx}]^*F[R_x] + F[g_{yx}]^*F[R_y]\right\} \tag{8c}$$

and

$$R_y(i,j) - s_y(i,j)\chi_2^*(i,j)R_y(i,j) - \chi_4^*(i,j)F_{ij}^{-1}\left\{F[g]^*F[R_y]\right\} - \chi_2^*(i,j)F_{ij}^{-1}\left\{F[g_{xy}]^*F[R_x] + F[g_{yy}]^*F[R_y]\right\} \tag{8d}$$

where $0 \leq i \leq m_1 - 1$ and $0 \leq j \leq m_2 - 1$. In (8) D_μ and R_μ are $n_1 \times n_2$ two-dimensional arrays with $n_1 \geq 2m_1 - 1$, $n_2 \geq 2m_2 - 1$, and both n_1 and n_2 being integer powers of 2. Arrays $D_\mu(i,j)$ and $R_\mu(i,j)$, with $0 \leq i \leq m_1 - 1$ and $0 \leq j \leq m_2 - 1$, correspond to the auxiliary correction and residue vectors used in the CGM, respectively, and $D_x(i,j) = D_y(i,j) = R_x(i,j) = R_y(i,j) = 0$ when $i \geq m_1$ or when $j \geq m_2$ [5]. The symbol F denotes an FFT operating on $n_1 \times n_2$ two-dimensional arrays, and F_{ij}^{-1} denotes the ith row and jth column element of the resulting array after the inverse FFT. The asterisk superscript denotes complex conjugate. In writing (8c) and (8d), we have made use of the property $F[f^*(-i,-j)] = F[f(i,j)]^*$, where f is an arbitrary $n_1 \times n_2$ two-dimensional (periodic) array [16]. It is seen that the computations in (8) require 12 $n_1 \times n_2$-point FFT's. Note that the memory requirement is linearly proportional to the total number of unknowns.

V. Condition Number of the Matrix

The equations in (5) can be written in the form of the matrix equation

$$\boldsymbol{A}\boldsymbol{x} = \boldsymbol{b} \tag{9}$$

where the vectors $\boldsymbol{x}$ and $\boldsymbol{b}$ denote the unknown and incident fields, respectively. The condition number c of matrix $\boldsymbol{A}$ is a measure of the sensitivity of the solution $\boldsymbol{x}$ with respect to the errors in $\boldsymbol{A}$ or $\boldsymbol{b}$. Quantitatively, this number is given by the product [see, for example, 17, ch. 9]

$$c = \|\boldsymbol{A}\| \cdot \|\boldsymbol{A}^{-1}\| \tag{10}$$

where $\|\boldsymbol{A}\|$ and $\|\boldsymbol{A}^{-1}\|$ are the spectral norms of matrix $\boldsymbol{A}$ and its inverse, and are equal to the square roots of the largest and smallest eigenvalues of the composite matrix $\tilde{\boldsymbol{A}}\boldsymbol{A}$ ($\tilde{\boldsymbol{A}}$ being the transpose and complex conjugate of matrix $\boldsymbol{A}$), respectively. A quick way to estimate the spectral norm of a matrix $\boldsymbol{A}$ is to calculate the Euclidean norm $\|\boldsymbol{A}\|_e$ and the maximum column-sum norm $\|\boldsymbol{A}\|_1$, where $\|\boldsymbol{A}\|_e$ = the square root of the sum of all the magnitudes of the matrix elements and $\|\boldsymbol{A}\|_1 =$

TABLE I
COMPARISON OF CONDITION NUMBERS, c, OF THE MATRICES RESULTING FROM TWO FORMULATIONS OF THE EFIE

		Conventional Method			Present Method		
ϵ	Δ/λ	$\|A\|$	$\|A^{-1}\|$	c	$\|A\|$	$\|A^{-1}\|$	c
2	0.04	1.943	1.072	2.08	1.073	2.153	2.31
10	0.01	9.503	1.291	12.27	1.127	8.567	9.65
100	0.004	94.570	1.666	157.58	1.115	23.674	26.40
1000	0.001	945.256	1.792	1694.03	1.115	27.219	30.36

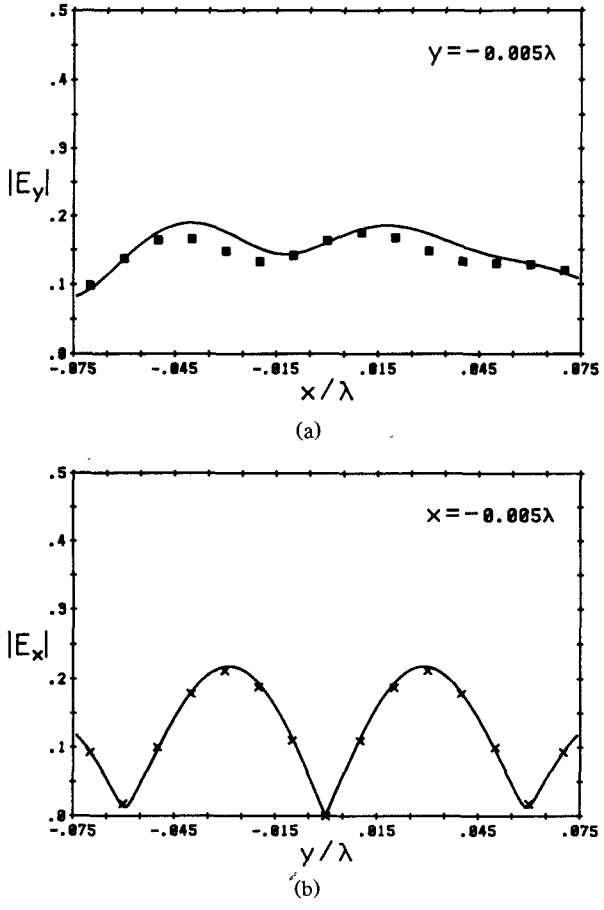

Fig. 3. Field distributions inside the circular cylinder of radius 0.075λ. The solid lines are the exact solutions; the squares or crosses are the calculated results.

$\max\{s_1 s_2 \cdots s_n\}$, s_j denoting the sum of the magnitudes of the elements in the jth column and n being the order of matrix A. Both of these two norms are upper bounds of the spectral norm. In addition, lower bound of the spectral norm can be found [17, ch. 1]. Thus, one has

$$\frac{1}{\sqrt{n}}\|A\|_e \leq \|A\| \leq \|A\|_e, \|A\|_1. \tag{11}$$

Thereby, it can be expected that the spectral norm will become large (small) when most of the magnitudes of the matrix elements are large (small).

To calculate the spectral norms of A and its inverse, we use the tridiagonalization and Sturm sequence [17, ch. 10] to solve for the eigenvalues of the composite matrix $\bar{A}A$. In doing this the matrix must be formed explicitly. We also apply the power method and the inverse power method [17, ch. 10] to check the results. It takes much more computation to find the condition number than to solve the EFIE. Thus, only small cases are treated in this section. Consider a homogeneous dielectric cylinder with a square cross section modeled by 3×3 cells. In the calculation we set $m_1 = m_2 = 4$ and $\Delta x = \Delta y = \Delta$. Four cases with various relative permittivities ϵ and ratios Δ/λ (λ being the free-space wavelength) are considered in Table I. For a direct comparison, the results of the matrices resulting from both the conventional [5] and the present method are given. It is seen that the norm $\|A\|$ of the conventional method *increases almost linearly* with the permittivity ϵ, when ϵ is large. This is because the magnitudes of the off-diagonal elements are roughly proportional to the permittivity ϵ [5] and are large enough to dominate the norm $\|A\|$. In contrast to this, the magnitudes of the off-diagonal elements in the present method are kept small and, together with those of the diagonal elements, are slowly varying with the magnitude of the permittivity. Consequently, the norm $\|A\|$ of the present method is kept *almost constant*, regardless of the magnitude of the permittivity. Unexpectedly, it is seen that the norm $\|A^{-1}\|$ of the present method increases somewhat with the permittivity. Thus, the condition number degrades somewhat as the permittivity is increased.

VI. NUMERICAL RESULTS

In order to check the accuracy of the proposed method, we consider the TE scattering by a circular homogeneous dielectric cylinder. The incident field is assumed to be $E^i = \hat{y}\exp(-jkx)$. The relative permittivity of the cylinder is chosen to be as large as 100. Actually, we use the staircase approximation in our calculation for the circular cylinder. To comply with the FFT algorithm we use 16×16 square cells ($m_1 = m_2 = 16$ and $n_1 = n_2 = 32$) in the calculation. But the cells outside the cylinder are filled just with air (vacuum). The total number of unknowns is 512, the maximum value executable on our present personal computer.

The field distributions near the x and y axes inside a circular cylinder are shown in Fig. 3, where the center of the cylinder is placed at the origin of the $x-y$ plane. The radius is 0.075λ and the corresponding cell's side length Δ is 0.01λ (λ being the free-space wavelength). Since the relative permittivity is 100, the cylinder's radius corresponds to 0.75 internal wavelength and the Δ corresponds to choosing ten node points per internal wavelength. Also shown in the figures are the exact solutions [18]. It is seen that the agreement is reasonably good. Note that for a scatterer with such a large permittivity, the conventional procedure for the block model [5] does not converge at all when the CGM is used, or yields entirely unreliable results when a direct method is used (as shown by the results in [8]). Since the CGM is an iterative method, one has to estimate the solution initially. In this investigation, incident fields were used as the starting functions. It is understood that the incident field behaves quite differently from the final solution, when the permittivity is large. For the case in Fig. 3, the number of iterations necessary for the CGM to reach convergence (the norm of residue $<10^{-4}$) is 175. This number is much smaller than 512, which is another indication of the condition numbers of the corresponding matrix being small. For larger radii it is seen that the convergence rates slow down and the errors increase significantly.

VII. CONCLUSION

Face-centered node points have been incorporated into the numerical procedure for solving the EFIE using the simple and efficient pulse-basis block model. By properly choosing the

unknown fields, the condition numbers of the resulting matrices are kept relatively small even when the permittivity is large. Compared with the exact solutions, it is seen that the accuracy is reasonably good.

It is seen that the norm $\|A^{-1}\|$ of the present method increases somewhat with the permittivity. The condition number of the matrix will be improved further if this norm can be reduced.

References

[1] J. H. Richmond, "Scattering by a dielectric cylinder of arbitrary cross section shape," *IEEE Trans. Antennas Propagat.*, vol. AP-13, pp. 334–341, May 1965.

[2] J. H. Richmond, "TE-wave scattering by a dielectric cylinder of arbitrary cross-section shape," *IEEE Trans. Antennas Propagat.*, vol. AP-14, pp. 460–464, July 1966.

[3] D. E. Liversay and K. M. Chen, "Electromagnetic fields induced inside arbitrarily shaped biological bodies," *IEEE Trans. Microwave Theory Tech.*, vol. MTT-22, pp. 1273–1280, Dec. 1974.

[4] D. T. Borup and O. P. Gandhi, "Calculation of high-resolution SAR distribution in biological bodies using the FFT algorithm and conjugate gradient method," *IEEE Trans. Microwave Theory Tech.*, vol. MTT-33, pp. 417–419, May 1985.

[5] C. C. Su, "Calculation of electromagnetic scattering from a dielectric cylinder using the conjugate gradient method and FFT," *IEEE Trans. Antennas Propagat.*, vol. AP-35, pp. 1418–1425, Dec. 1987. (The $\bar{\epsilon}$ and $W(\phi)\lambda$ in (7) and (23b) therein are misprints of $\bar{E}$ and $W(\phi)/\lambda$, respectively.)

[6] C. C. Su, "Electromagnetic scattering by a dielectric body with arbitrary inhomogeneity and anisotropy," *IEEE Trans. Antennas Propagat.*, vol. 37, pp. 384–389, Mar. 1989.

[7] A. F. Peterson and R. Mittra, "Convergence of the conjugate gradient method when applied to matrix equations representing electromagnetic scattering problems," *IEEE Trans. Antennas Propagat.*, vol. AP-34, pp. 1447–1454, Dec. 1986.

[8] D. T. Borup, D. M. Sullivan, and O. P. Gandhi, "Comparison of the FFT conjugate gradient method and the finite-difference time-domain method for the 2-D absorption problem," *IEEE Trans. Microwave Theory Tech.*, vol. MTT-35, pp. 383–395, Apr. 1987.

[9] H. Massoudi, C. H. Durney, and M. F. Iskander, "Limitations of the cubical block model of man in calculating SAR distribution," *IEEE Trans. Microwave Theory Tech.*, vol. MTT-32, pp. 746–752, Aug. 1984.

[10] M. J. Hagmann, H. Massoudi, C. H. Durney, and M. F. Iskander, "Comments on 'Limitations of the cubical block model of man in calculating SAR distribution'," *IEEE Trans. Microwave Theory Tech.*, vol. MTT-33, pp. 347–350, Apr. 1985.

[11] S. C. Hill, C. H. Durney, and D. A. Christensen, "Numerical calculations of low-frequency TE fields in arbitrarily shaped inhomogeneous lossy dielectric cylinders," *Radio Sci.*, vol. 18, pp. 328–336, May 1983.

[12] D. H. Schaubert, D. R. Wilton, and A. W. Glisson, "A tetrahedral modeling method for electromagnetic scattering by arbitrarily shaped, inhomogeneous dielectric bodies," *IEEE Trans. Antennas Propagat.*, vol. AP-32, pp. 77–85, Jan. 1984.

[13] C. T. Tsai, H. Massoudi, C. H. Durney, and M. F. Iskander, "A procedure for calculating fields inside arbitrarily shaped inhomogeneous dielectric bodies using linear basis functions with the moment method," *IEEE Trans. Microwave Theory Tech.*, vol. MTT-34, pp. 1131–1138, Nov. 1986. (For comments, see vol. MTT-35, pp. 785–786, Aug. 1987.)

[14] C. C. Su, "Fast algorithm for transversely inhomogeneous optical fibres using power method and fast Fourier transform," *Proc. Inst. Elec. Eng.*, vol. 134, pt. J, pp. 276–280, Oct. 1987.

[15] C. C. Su, "A surface integral equations method for homogeneous optical fibers and coupled image lines of arbitrary cross sections," *IEEE Trans. Microwave Theory Tech.*, vol. MTT-33, pp. 1114–1119, Nov. 1985.

[16] A. V. Oppenheim and R. W. Schafer, *Digital Signal Processing*. Englewood Cliffs, NJ: Prentice-Hall, 1976, p. 110.

[17] A Ralston and P. Rabinowitz, *A First Course in Numerical Analysis*, 2nd ed. New York: McGraw-Hill, 1978.

[18] R. Harrington, *Time-Harmonic Electromagnetic Fields*. New York: McGraw-Hill, 1961, p. 261.

A Dipole Antenna for Interstitial Microwave Hyperthermia

W. Hürter, F. Reinbold, and W. J. Lorenz

Abstract—**An improved interstitial microwave antenna design was investigated in static phantom experiments at 915 MHz and different insertion depths. Compared with conventional interstitial antennas, the dipole microwave antenna presented in this paper shows heating patterns which are concentrated on the dipole irrespective of the insertion depth. By analogy to interstitial radiotherapy, the microwave antenna we have developed thus allows a high concentration of energy in the target volume with as little damage as possible to the healthy surrounding tissue. The undesired heating of healthy tissue along the feeding line observed with conventional interstitial antennas is avoided. A $\lambda/4$ sleeve on the feeding line (which does not radiate microwave energy itself to the surrounding tissue) transforms an open end, i.e., a high impedance at the generator end of the dipole antenna. The current flowing back along the outside of the outer conductor of the feeding line in the direction of the generator is 0 at this point. Both dipole sections thus have the same terminating impedance. Since the $\lambda/4$ sleeve is mounted outside the antenna, its mechanical length is not restricted by the mechanical length of the antenna. It can hence be charged with dielectric materials of low dielectricity constants, e.g. PTFE.**

I. Introduction

Results from basic research and clinical investigations show that hyperthermia in combination with radiotherapy is an effective means of treating cancer [1]–[4]. In addition, many of these results demonstrate that the level of hyperthermic cytotoxicity and the sensitization of the tumor tissue to radiotherapy rise exponentially with temperature [5], [6]. The result of treatment thus crucially depends on the capacity of the hyperthermia system to attain a controlled temperature hyperelevation of the entire target volume [7], [8]. Interstitial microwave antennas are especially suitable for inducing hyperthermia of deep-seated tumors (e.g. certain brain tumors), since a homogeneous distribution of electromagnetic energy in the target volume also entails the expectation of an almost homogeneous stable temperature hyperelevation in the target volume except when there are major temperature gradients in the vicinity of large vessels. A "thermal washout" by flow of blood, such as can be observed in the use of ferromagnetic seeds or radio frequency needles, occurs to a much lesser extent here [9]. Inter alia, the distribution of the electromagnetic field can be adapted to the respective target volume by the form and arrangement of the interstitial microwave antennas. The plastic catheters used in interstitial combination therapy (radiotherapy/hyperthermia) can be used to accommodate both, e.g. radioactive iodine seeds and microwave antennas.

Manuscript received July 16, 1990; revised December 19, 1990. This work was supported by the Deutsche Krebshilfe.

The authors are with the Department of Radiology and Pathophysiology, German Cancer Research Center, Heidelberg, Germany.

IEEE Log Number 9144270.